

An improved mining image segmentation with K-Means and morphology using drone dataset

Nasreddine Haqiq¹, Mounia Zaim¹, Mohamed Sbihi¹, Mustapha El Alaoui², Lhoussaine Masmoudi², Hamza Echarrafi³

¹Laboratory LASTIMI, High School of Technology Sale, Mohammed V University in Rabat, Rabat, Morocco

²LCS Laboratory, Physics Department, Faculty of Sciences, Mohammed V University in Rabat, Rabat, Morocco

³SGMG Company, Co-Founder, Kenitra, Morocco

Article Info

Article history:

Received Oct 23, 2023

Revised Feb 23, 2024

Accepted Feb 25, 2024

Keywords:

Drone technology

Image processing

Image segmentation

K-Means clustering

Mining 4.0

Mining industry

ABSTRACT

The mining industry faces the challenge of incorporating advanced technology to explore new ways of increasing productivity and reducing costs. Our focus is on integrating drone technology to revolutionize mining tasks like inspection, mapping, and surveying. Drones offer a precision advantage over traditional satellite methods. To this end, we have created a dataset consisting of 373 aerial images captured by a DJI Phantom 4 drone, which depict a mining site in the Benslimane region of Western Morocco. These images, with a ground resolution of 2.5 cm per pixel, are the basis of our research. Our study aims to address the challenges posed by traditional mining techniques and to leverage technological innovations to improve segmentation and classification. The proposed approach includes new methodologies, particularly the combination of K-Means clustering and mathematical morphology, to overcome limitations and deliver better segmentation results. Our findings represent a significant step forward in advancing mining operations through the effective use of modern technologies.

This is an open access article under the [CC BY-SA](#) license.



Corresponding Author:

Nasreddine Haqiq

LASTIMI Laboratory, High School of Technology Salé, Mohammed V University in Rabat

Rabat, Morocco

Email: nasreddine_haqiq@um5.ac.ma

1. INTRODUCTION

The use of drone technology for industrial applications debuted in July 1849 with a balloon carrier, marking the initial naval aviation airpower used for remote sensing [1]. The origin of drones was developed around the beginning of the First World War in 1917 and 1918 by British drones. A drone is a flying object that can fly by itself with a remote control or by installing a software development kit to draw the trajectory on a smartphone, on a commercial platform, or without a pilot. In the United States, the term is defined as unmanned aircraft systems; it was adopted by the Department of Defense and the Federal Aviation Administration [2]. Unmanned aerial vehicles can survey inaccessible areas without risking the safety of humans and require image processing for converting images to 3D data. Recently, the research and development of drones have been growing due to multiple investments by companies and demand in markets [3]–[5].

The mining sector has shown an increase in demand for drones with high-resolution sensors that are being used for the inspection of large structures and to reduce human risks. It is replacing the classic visual inspection [6]. Mining operations changed radically with digital technologies because of Industry 4.0, which affected the mining industry. Nowadays, it is called mining 4.0, a mining operation in which a miner can

oversee the real-time production process, conduct data analysis, and contribute to decision-making [7].

Various studies show the use of drones in the mining industry. In their article, Ren *et al.* [5] reviewed a case of using drones for mine operations such as site supervision, surveying, 3D models, pollution monitoring, and land damage evaluation. Esposito *et al.* [8] describe a geomatic approach to assess changes in surface mine extension, quantify excavated volume, and produce 3D point cloud spatial data by acquiring multi-temporal images for an open-pit mine in Sardinia, Italy.

The term mining 4.0 appeared in the 4th industrial revolution. It improves mining operations and the metals industry through digital technologies and data analytics technologies. Those technologies provide automated decision-making for machines, equipment, and operations. Digital transformation and automated mining offer productivity, safety, and efficiency. It aims to optimize the entire mining value chain, from step one, which is exploration and extraction, to the last step, processing, and transportation, by leveraging data-driven insights and real-time decision-making. The objective of Mining 4.0 is to create a more profitable and sustainable mining industry by reducing costs, improving safety, and minimizing environmental impact. Figure 1 shows the impact of digital transformation and mine automation on optimizing operations.

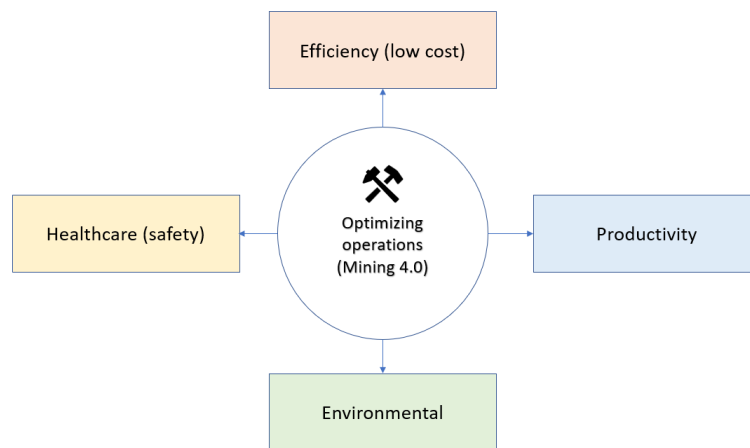


Figure 1. The impact of digital transformation and mine automation in optimizing operations

Our research is focused on a new method for image segmentation by merging the K-Means clustering algorithm with mathematical morphology. While K-Means is a widely used algorithm for image segmentation, we have innovatively integrated mathematical morphology to form a hybrid method. This integration overcomes the limitations of traditional K-Means and delivers superior segmentation outcomes. The fusion of K-Means and mathematical morphology enhances our understanding of image features, resulting in more accurate segmentation. Our contribution involves creating a novel approach that extends the utility of K-Means, resulting in a potential breakthrough for better image segmentation across various applications. The research also aims to examine the application of unmanned aerial vehicle technology in the mining industry using a segmentation approach. This paper will define mining 4.0 and the segmentation method. The three-dimensional point cloud, orthophoto, and mesh3D were produced using drone image capture.

We presented an article that includes the following sections: in section 2, we explain our proposed method, which combines mathematical morphology and K-Means clustering. In section 3, we discuss our study sites, data collection, and the process of generating 3D point clouds. In section 4, we discuss the results of our study, including the digital model elevation, insights gathered from 3D point cloud analysis, and outcomes of segmentation using K-Means clustering and mathematical morphology. Finally, we conclude our study in section 5 by summarizing our findings and presenting our conclusive remarks.

2. THE PROPOSED METHOD

This section introduces our methodology to address the challenge of segmenting drone-captured images in the mining sector. Our proposed approach combines the techniques of K-Means clustering and math-

emational morphology to achieve accurate segmentation. Initially, K-Means is applied to segment the image based on color or intensity similarities, providing an initial partition of the image into distinct regions. To further improve the segmentation quality, we employ mathematical morphology, which allows us to refine the boundaries and effectively remove small artifacts that might have been introduced during the initial clustering step. By integrating these two techniques, we aim to enhance the overall segmentation results, ensuring a more precise representation of regions of interest in the mining images. The proposed method is followed as Figure 2.

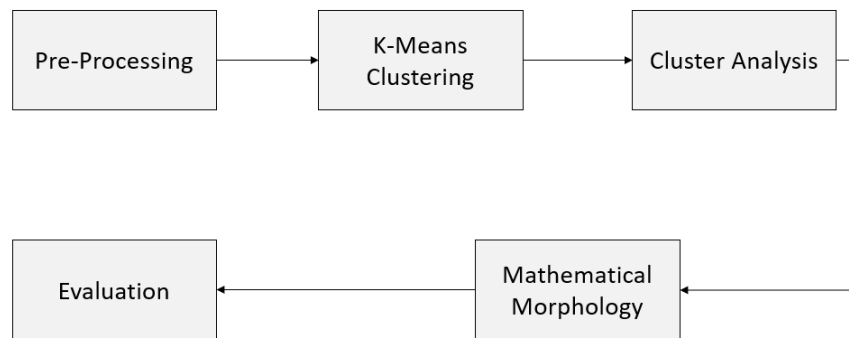


Figure 2. Block diagram of the proposed method

- Pre-processing: In this step, we will apply the necessary pre-processing steps like noise reduction [9] and contrast enhancement to improve the image quality.
- K-Means clustering: We perform the algorithm on the pre-processed image (step 1) by converting the red-green-blue (RGB) to lightness (L), red-green (A), and yellow-blue (B) (LAB) color space. The LAB color space is better than the RGB color space for image segmentation and processing tasks. It has advantages, especially in the color separation (A and B components) from the lightness (L component). The separation is beneficial for image segmentation that relies on color differences. The K-Means algorithm will allow segmentation according to color and intensity similarities. The K is determined according to the number of regions or objects we wish to segment. Waskale [et al. [10] comparison of RGB and CIEL*a*b* shows that CIEL*a*b* (LAB color space) was more suitable for measuring the color of fresh or dried fruits and vegetables. The RGB-regenerated color shows better color saturation than the LAB color space. Still, the total color variation from set to set of tested fruits and vegetables was possible to predict only with the LAB color space coordinates.
- Cluster analysis: analyze the results of K-Means clustering (Step2) and identify the cluster that corresponds to the region or object you wish to segment. This involves examining cluster centroids, cluster histograms, or other cluster characteristics.
- Mathematical morphology: we are applying the mathematical morphology operations to the segmented image to improve the quality of segmentation obtained from the initial process. Using erosion, it is possible to slightly reduce the size of segmented regions, which can be particularly useful to eliminate the isolated pixels that could be due to noise. On the other hand, the dilation could be used to enlarge segmented areas, filling in small gaps between objects of interest. In addition, the opening operation, involving a sequence of erosions followed by dilations, is frequently employed to smooth the contours of the zone and eliminate the small asperities. This process results in more uniform, better-defined boundaries for each segment. Conversely, closure, the opposite of opening, can be used to fill small cavities in the zones and ensure the continuity of the segments. The underlying aim is to improve the accuracy and quality of the segmentation by eliminating minor imperfections and enhancing contour coherence, fundamental elements for multiple applications in image processing.
- Evaluation: evaluate the performance of the method and compare the results with the classical approach to determine better segmentation. The proposed method can be represented as an algorithm, which is described in algorithm 1.

Algorithm 1. The proposed method algorithm

```

1: procedure KMEANSMORPHOLOGY( $I, K, SE$ , Morphological Operation, Iterations)
2:   Input: Image  $I$ , Number of clusters  $K$ , structuring element  $SE$ 
3:   Morphological operation (Dilation or Erosion), Iterations for K-Means and Morphology
4:   Output: Segmented Image
5:   1. Preprocess the input image  $I$ :
6:     a. Convert  $I$  to LAB color space.
7:     b. Extract the relevant channels ( $a^*$  and  $b^*$ ).
8:   2. Apply K-Means Clustering:
9:     a. Reshape the 2D array of pixels to a 1D array.
10:    b. Run K-Means clustering with  $K$  clusters.
11:    c. Reshape the resulting cluster assignments to a 2D array.
12:   3. Apply Morphological Operations:
13:     a. Create binary masks for each cluster using K-Means results.
14:     b. Apply the chosen morphological operation (Dilation or Erosion) to each mask using  $SE$ .
15:     c. Combine the morphological results to get the final segmentation.
16:   4. Display and save the segmented image.
17:   Example Usage:
18:     Input: Image  $I$ ,  $K = 3$ ,  $SE$ , Dilation, Iterations=5
19:     Output: Segmented Image
20: end procedure

```

3. MATERIAL AND METHODS

To conduct our study, the first step is to identify the study site. This involves carefully selecting and defining the geographical area being investigated, taking into consideration the environmental conditions and relevance to our research objectives. Once the site has been identified, the next critical steps involve acquiring data and processing images. Our methodology relies heavily on 3D spatial information derived from drone images. This comprehensive approach aims to capture a detailed representation of the study area, enabling us to conduct a thorough analysis of its features. The data collected from this process will then undergo meticulous processing, and the results obtained will form the foundation for the subsequent stages of our study. This ensures a smooth integration of both data gathering and analytical procedures, leading to a robust and systematic investigation. Please refer to Figure 3 for a visual representation of our study process.

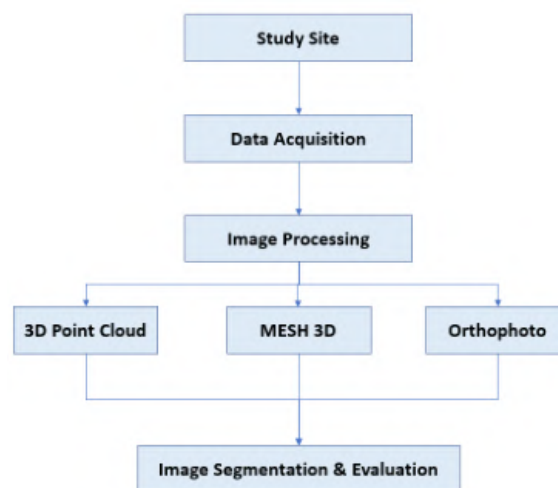


Figure 3. Study flow of data acquisition and image processing for image segmentation and evaluation analysis

3.1. Study site

The study area is a mining site located in the Benslimane region, to the west of Morocco. It has a latitude of -7.02, a longitude of 33.64, and an altitude of 398 meters. For the analysis, only the important mining locations were selected and images were taken. Figure 4 displays the Google satellite and OpenStreetMap (OSM) views of the area, while Table 1 provides details on the weather conditions during data acquisition. Additionally, for this study, a dataset was collected and made available through Mendeley data [11].

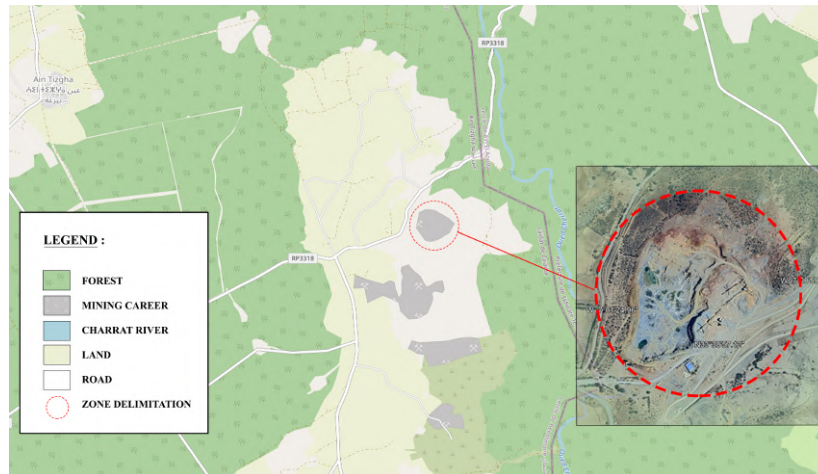


Figure 4. Study location in Benslimane region of Morocco

Table 1. Weather conditions during the acquisition

Humidity	Weather condition	Temperature (C)	Wind condition	Wind speed (Km/h)
76	Partly clear	20-24	Light breeze	4-14

3.2. Image acquisition by drone

The images were captured by the drone Da Jiang Innovation (DJI) Phantom 4 Pro as shown in Figure 5 on June 8, 2022, to analyze changes in the environment and to do an inspection of the area. The images were captured from an altitude of 398 meters in the middle part of the mine. 15 percent of the parts were remote controlled due to environmental issues, and the rest are automatic paths configured on DJI Phantom 4 parameters. Figure 6 shows all the positions where the DJI Phantom 4 Pro took pictures, while Table 2 displays the parameters of the drone and camera characteristics. In total, 373 images were captured by the drone, with each picture being 8.28 MB in size and having a quality of 4K. This resulted in a total of 3.016 GB of space being used to store the images.



Figure 5. Drone DJI Phantom 4 Pro in the study site



Figure 6. Drone trajectory with Google satellites and OSM maps [7]

Table 2. Shows the parameters of the drone and the camera characteristics

Drone	Dji Phantom 4 Pro
Model	FC6310R
Image resolution	5472x3648
Flight time	30 min
Weight	3.5 KG
Size for one image	8.41 MB
bits compressed by pixel	3.42
Presentation of colors	RGB
Color depths	24 bits per pixel

3.3. Data acquisition and point cloud calculation

To produce our spatial data, we used a commercial product called Agisoft Metashape Professional [12]. This software is a leading photogrammetry tool for drone mapping. Our evaluation includes assessing the quality of point cloud resolution, 3D modeling, and orthophoto to precisely analyze and enhance the digital elevation model and point cloud files. In Figure 7, you can see some of the photos captured by a Drone DJI Phantom 4 Pro.



Figure 7. Example of drone photos captured by DJI Phantom 4 Pro

After the image acquisition, there are 3 steps to create the point cloud 3D using Agisoft Metashape:

- First step: select all the 373 images captured and configure the coordinate system to WSG 84 (ESPG:4326) with rotation angle yaw, pitch, and roll.
- Second step: align all the photos together to make it one object so we can have points stuck to each other.
- Third step: create point cloud 3D with total of 216.327 points.

Figure 8 shows the orthophoto of the study area. The orthophoto method allows for orthorectifying the digital image and registering it to a coordinate map projection. It transforms an image into a sensor geometry for cartographic projections.



Figure 8. Orthophoto of the study area

Once the three steps are completed, the software generates a point cloud, which is saved as a Log ASCII Standard (LAS) extension file. The LAS format, created by the American Society for Photogrammetry and Remote Sensing (ASPRS) in 2011 [13], is used to compress the file size and optimize it instead of using the heavier XYZ extension. Table 3 provides a comparison of file sizes between LAS format (ASPRS – 2011), object format, and XYZ format. To generate the dataset and complete the process of 216327 points, we used a computer with Windows 11 as the operating system, an AMD Ryzen 7 3700U with Radeon Vega Mobile GFX, 12 GB DDR4 RAM, and 1 TB of Solid State Drive.

Table 3. Comparison between the three format of 3D point cloud and 3D format

Filename	File size in [MB]	File size compressed (RAR)	*Time of process (minutes)
Benslimane_point_cloud.las	6.124 MB	4 MB	25 minutes
Benslimane_point_cloud.txt	15.125 MB	6 MB	25 minutes
Benslimane_3D.obj	6.443 MB	5.9 MB	58 minutes

4. RESULTS AND DISCUSSION

4.1. Point cloud and data visualization

The point cloud was generated by following a set of well-defined procedures. Figure 9 shows the resulting three-dimensional point cloud, which accurately represents spatial information. The point cloud consists of a total of 216,327 points, separated into two segments. The first segment of the point cloud is made up of data from 189 images, while the second segment includes data from 184 images. This approach not only ensures a comprehensive spatial representation but also facilitates a more nuanced understanding of the underlying structures and features within the dataset.

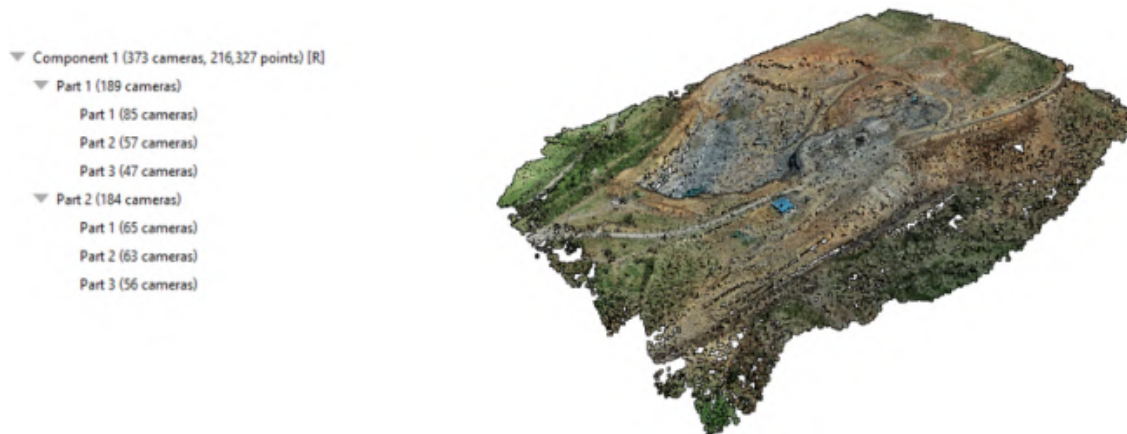


Figure 9. Result of the point cloud processing

For visualization of this dataset, the Web Graphics Library browsers of 3D spatial data render numerous points; for example, Potree (Markus Schütz) [14], is an open source Web Graphics Library browser and desktop application point cloud that contains Potree converter [15]. This converter is made with the octree generation method, which is the most optimized, has fast rendering, splits the point cloud into small chunks, and makes the point cloud structured [16]. Figure 10 shows the result of point cloud 3D visualization using a Potree viewer.

The number of points in a point cloud 3D rendering is 216,327, but the actual number of points generated is 246,659. The difference between the two is called tie points, which are duplicate points. The imprecision in tie points can be calculated as follows: Tie Points imprecision: $246,659 - 216,327 = 30,332$ points. These 30,332 tie points are common objects between two different images. After the alignment step, only the 216,327 valid tie points are used, while the 30,332 tie points are disabled due to their imprecision. Table 4 provides information about the tie points and alignment parameters.



Figure 10. Result of 3D point cloud visualization using Potree Viewer

Table 4. The tie points and alignment parameters

	Name	Value
Tie Points	Points	216,327 of 246,659
	Point Colors	3 bands
	Point Colors Type	uint8
	Average tie Point Multiplicity	6666
	Point Colors	3 bands
Alignment Parameters	Accuracy	High
	Key point limit	40000
	Exclude stationary tie point	Yes
	Matching time	17 minutes 52 seconds
	Matching memory usage	2.77 GB
	Alignment time	4 minutes 49 seconds
	Alignment memory usage	150.86 MB

4.2. Digital elevation model (DEM)

The digital elevation model (DEM) is a representation of the terrain without any buildings, trees, or other objects [17]. It can be generated using sparse point cloud, dense point cloud, or depth maps. In this study, the size of the DEM is 1092x968 pixels, and it took 6 seconds to produce with interpolation enabled. Figure 11 displays the result of the DEM, which has a resolution of 1.26m/pix.

After producing the DEM, we save it in GeoTIFF (TIF) format. To optimize its analytical capabilities, we open the DEM with Rasterio[18], read the array, and convert it to a floating-point format. Using Matplotlib, we create two subplots displaying the DEM: one in a bone color scheme for elevation differences and another with a rainbow color map and contour lines for detailed terrain features. Additionally, we employ Richdem [19] for advanced terrain analysis, extracting specific characteristics from the DEM. The integration of RasterIO and Richdem enhances our geospatial study, enabling comprehensive processing and interpretation of terrain features.

In Figure 12, we are using a compelling visualization of the DEM TIF report. With colormap, this visualization gives a vibrant representation of the terrain's elevation attributes. The preference for colormap enables intensifying variations in elevation, making it less difficult to discern the tricky information of the panorama. This step is pivotal in our geospatial analysis workflow because it permits us to advantage of precious insights into the topography and plan. In the next step, we convert the image into a rainbow-colored visual representation. Then, we use a tool called the contour process to analyze the DEM by accurately identifying points within the raster image.

The results of this transformation are depicted in Figure 13. The first figure shows the DEM using a rainbow color palette, which allows us to visualize elevation variations. The second figure provides a zoomed-in view, highlighting specific features of the image through the contour details. This step holds great importance in our analysis process, as it provides us with a better understanding of the topography and significant features of the area being studied.

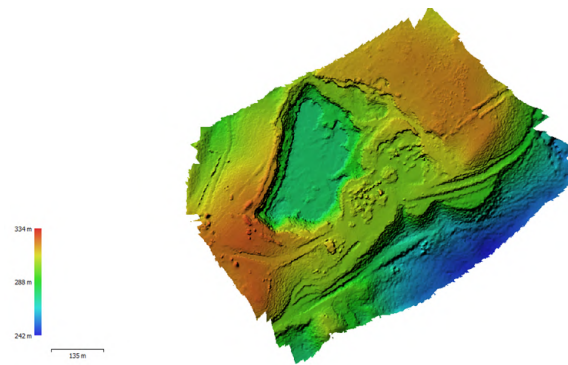


Figure 11. Result of DEM with 1.26 m/pix

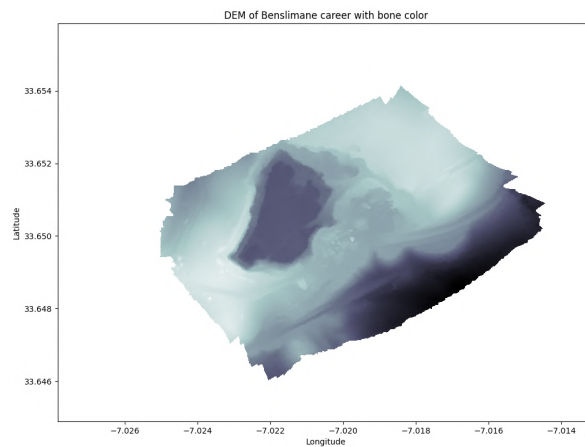


Figure 12. Output of DEM Benslimane TIF file with bone as colormap

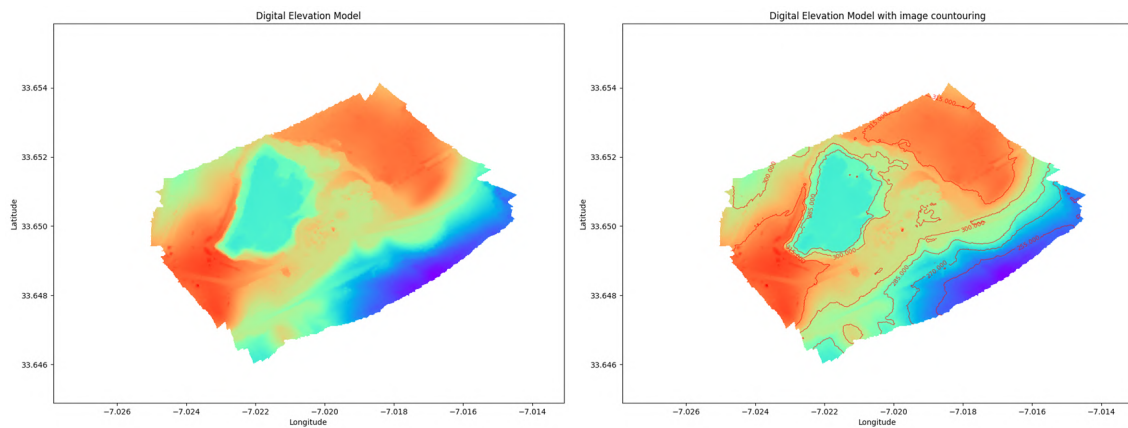


Figure 13. The output of digital elevation model and with the contouring

4.3. Analysis of accuracy and calibration coefficients

The accuracy of 3D spatial data information of Benslimane mine is generated during the drone images and analyzed with a total of 10 checkpoints (CP), The values of each dataset are X, Y represents the plan as longitude and latitude, and the Z value represents an elevation difference at the (X, Y) coordinate pair. The calculation of the root mean square error [20] is divided by X, Y, and Z using (1):

$$\text{RMSE} = \sqrt{\frac{1}{n} \sum_{i=1}^n (v_i)^2} \quad (1)$$

where:

$$v_i = v_{\text{Surveyed}} - v_{\text{Measured}} \quad (2)$$

And for the equation for x, y, and z :

$$\text{RMSE}_{(r)}(r = x, y, z) = \sqrt{\frac{1}{n} \sum_{i=1}^n (v_i)^2} \quad (3)$$

And n is the number of checkpoints. We can proceed with the calculation of the three coordinates:

$$\begin{aligned} \text{RMSE}_x &= \sqrt{\frac{(-0.05)^2 + (0.1)^2 + (-0.059)^2 + (-0.109)^2 + (0.082)^2 + (0.122)^2 + (0.108)^2 + (-0.06)^2 + (-0.096)^2 + (-0.108)^2}{10}} \\ &= 0.087 \text{ m} \end{aligned}$$

$$\begin{aligned} \text{RMSE}_y &= \sqrt{\frac{(-0.073)^2 + (0.106)^2 + (-0.058)^2 + (0.019)^2 + (0.122)^2 + (-0.054)^2 + (0.1)^2 + (0.032)^2 + (0.05)^2 + (-0.052)^2}{10}} \\ &= 0.073 \text{ m} \end{aligned}$$

$$\begin{aligned} \text{RMSE}_z &= \sqrt{\frac{(-0.07)^2 + (-0.07)^2 + (-0.13)^2 + (-0.16)^2 + (-0.06)^2 + (-0.1)^2 + (-0.16)^2 + (-0.12)^2 + (-0.08)^2 + (-0.13)^2}{10}} \\ &= 0.113 \text{ m} \end{aligned}$$

Table 5 contains information about the ten checkpoints with measured values, surveyed values, and residual values where:

$$\text{Residual Values} = \text{Surveyed Values} - \text{Measured Values}$$

Table 5. Results of calculating the root mean square error for measured, surveyed, and residual values of CP

	Value Measured			Value surveyed			Residuals		
	X	Y	Z	X	Y	Z	X	Y	Z
	m	m	m	m	m	m	m	m	m
CP1	683401337	3725214006	398.81	683401287	3725213933	398.74	-0.05	-0.073	-0.07
CP2	683597974	3724906922	398.85	683598074	3724907028	398.78	0.1	0.106	-0.07
CP3	683911476	3725158882	398.83	683911417	3725158824	398.7	-0.059	-0.058	-0.13
CP4	683767424	3725437683	398.8	683767315	3725437702	398.64	-0.109	0.019	-0.16
CP5	683683274	3725437731	398.75	683683356	3725437853	398.69	0.082	0.122	-0.06
CP6	683829007	3725371078	398.78	683829129	3725371024	398.68	0.122	-0.054	-0.1
CP7	683570321	3725197826	398.8	683570429	3725197926	398.64	0.108	0.1	-0.16
CP8	683485189	3725171457	398.81	683485129	3725171489	398.69	-0.06	0.032	-0.12
CP9	683649922	3725096401	398.85	683649826	3725096451	398.77	-0.096	0.05	-0.08
CP10	683478748	3725091126	398.78	683478.64	3725091074	398.65	-0.108	-0.052	-0.13
NB CP	10	10	10						
RMSE	0.087	0.073	0.113						

After calculating the easting (X), the northing (Y), and the elevation (Z), we will evaluate the improvement of measurements so the root mean square error (RMSE) can be near the objective. For example, the RMSE in easting is 0.087 m and may become 0.053 m with an improvement of 3.4 centimeters and this needs a human interaction for this decision to make this small adjustment, for the Northing, it needs an adjustment

from 0.073 to 0.067 m and no improvement in terms of elevation. Table 6 shows the average camera location errors of the drone Dji Phantom 4 Pro in meters.

Table 6. Camera error location average

X Error (m)	Y Error (m)	Z Error (m)	XY Error (m)	Total Error (m)
0.0537	0.06729	0.1752	0.0858	0.1951

With those results of RMSE, the calibration camera coefficients are identified as: i) F is the focal length in pixels; ii) Cx and Cy are point offset principal in pixel also; iii) The radial distortion coefficients are identified as K1, K2, and K3; and iii) Tangential distortion coefficients identified P1 and P2. The matrix in Table 7 is the correlation matrix from the camera coefficients [21]:

Table 7. The correlation matrix

	F	Cx	Cy	K1	K2	K3	P1	P2
F	1	0.82	-0.78	-0.99	0.98	-0.97	-0.85	0.82
Cx		1	-0.65	-0.82	0.81	-0.79	-0.78	0.67
Cy			1	0.77	-0.76	0.75	0.66	-0.77
K1				1	-0.99	0.98	0.86	-0.83
K2					1	-1	-0.84	0.81
K3						1	0.83	-0.8
P1							1	-0.71
P2								1

The correlation coefficient can vary from -1 to 1, 0 indicates that there is no linear relationship between the variables, and they are not correlated. 1 indicates a perfect positive linear relationship and -1 indicates a perfect negative linear relationship. In our matrix: i) The diagonal elements have a correlation coefficient of 1, which means that they are perfectly correlated with themselves; ii) The correlation between K1, K2, and K3 is approximately -1, indicating a perfect negative linear relationship; and iii) The correlation between P1 and P2 with other variables is low.

Those coefficients of the correlation matrix indicate a well-calibrated camera with accurate distortion parameters and results in a lower root mean square error also if there is a strong correlation between errors, it may indicate issues in calibration or the quality of the image.

4.4. Segmentation

4.4.1. Related works with improved K-Means clustering in the context of image

The algorithm K-Means is one of the simplest clustering algorithms used in machine learning and data analysis. It is an unsupervised learning algorithm that works by partitioning a set of data points into k-clusters and then assigning which cluster whose centroid (mean) is the closest to it. Numerous researchers are endeavoring to develop new methods that are more efficient than the current method and demonstrate a better-segmented result.

Yao *et al.* [22] proposed an improved image segmentation K-Means clustering algorithm. In this paper, they evaluate the proposed algorithm with a dataset of fish images comparing them with several segmentation methods, and then show the proposed algorithm outperforms other methods in terms of accuracy and robustness. In the proposed algorithm, the author uses a modified distance metric which is based on the L1 norm for better results to the background noise and color variation.

Qureshi *et al.* [23] introduced a method of image segmentation using K-Means clustering with neutrosophic Logic. The authors provided a detailed description of their related work which is about an approach that transforms an image into a neutrosophic set by calculating the truth, falsity, and determinacy values of each pixel. The image is pre-processed to remove noises, the neutrosophic transformation after that they use the K-Means clustering algorithm to cluster the neutrosophic values of each pixel into different groups and finally, the empty cluster is removed and merging clusters to remove all the empty clusters and improve the segmentation results. This methodology showed results that their approach outperformed the traditional K-Means with experiments on several images conducted by the authors.

Jardim *et al.* [24] proposed a method for graphical region extraction from images using K-Means clustering and watershed algorithm. In this article, authors apply K-Means clustering to group similar pixels in

the image and then the watershed to segment the images into regions based on cluster results. From the results, it can be concluded that their method performed better in efficiency.

Algorithm 2 presents the K-Means clustering approach to parallelized image segmentation. The first step takes as input image and the number of clusters, and then we load the pixel of data to convert it into a 2D array. At this stage, we initialize k cluster centroids equal to 3, 5, and 10. In each iteration, the pixels are assigned to the closest cluster centroid. The results of each batch are merged to obtain the final cluster labels. The pixels are replaced with the corresponding cluster color centroid, and the segmented pixels are reshaped into a 3D array. This algorithm leverages parallel processing to improve computational efficiency and is suitable for large-scale image segmentation tasks.

Algorithm 2. K-Means clustering algorithm

```

1: Input:
    • Image: the input image.
    •  $K$ : number of clusters.
    • max_iterations: the maximum iteration number for K-Means.
2: Output: Return segmented_image()
3: Load image
4: Convert image into a 2D array of pixels
5: Initialize the  $K$  cluster centroids
6: Divide the pixel data into multiple batches
7: for each iteration do
8:   For each batch, do the following steps in parallel:
9:     Assign pixel to the closest centroid
10:    Update each cluster centroid to be the mean of the pixels assigned
11: end for
12: Merge the results from each batch to obtain the final labels
13: Replace each pixel with its corresponding cluster centroid color
14: Reshape the segmented pixels into a 3D array
15: Return the segmented image

```

To begin explaining the proposed method, it is essential to first understand the application of mathematical morphology to the original image. This involves examining four main operations: dilation, erosion, opening, and closing. Dilation increases the size of object boundaries, while erosion reduces them. Opening and closing operations are useful for removing small objects and smoothing contours. Figure 14 provides a visual representation of these morphological operations. Figure 14(a) shrinks objects in the image, while Figure 14(b) expands them. Figure 14(c) combines erosion and dilation, and Figure 14(d) performs the opposite.

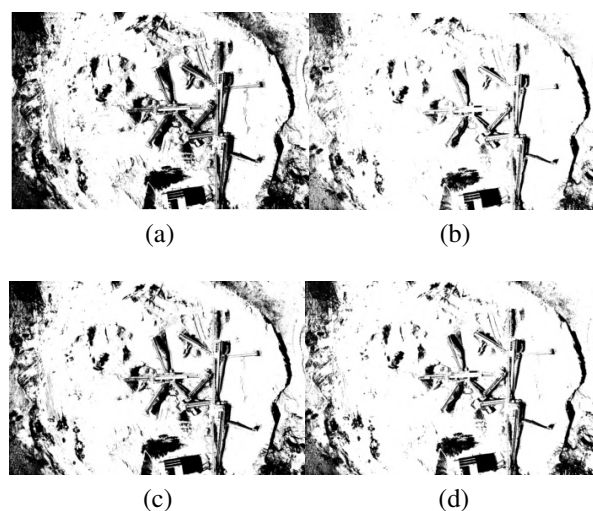


Figure 14. Mathematical morphology operations results on the original image (a) erosion, (b) dilation, (c) opening, and (d) closing

4.4.2. Segmentation results

In the context of our study, we used one original image that shows mining career equipment for the analysis. Mostly, the equipment is the area of interest, segmented from the background. Python is implemented to do all this work and for the comparison. We invoke the influential K-Means clustering algorithm, consciously selecting distinct $k=3$, $k=5$, and $k=10$. Before the K-Means step, we apply the noise reduction, the contrast enhancement, and the image conversion from RGB to LAB color space. Figure 15 displays outcomes for k values of 3 in Figure 15(a), 5 in Figure 15(b), and 10 in Figure 15(c). The original image is shown in Figure 15(d), the terrain mask in Figure 15(e), the equipment mask in Figure 15(f), and the segmented image results in Figure 15(g).

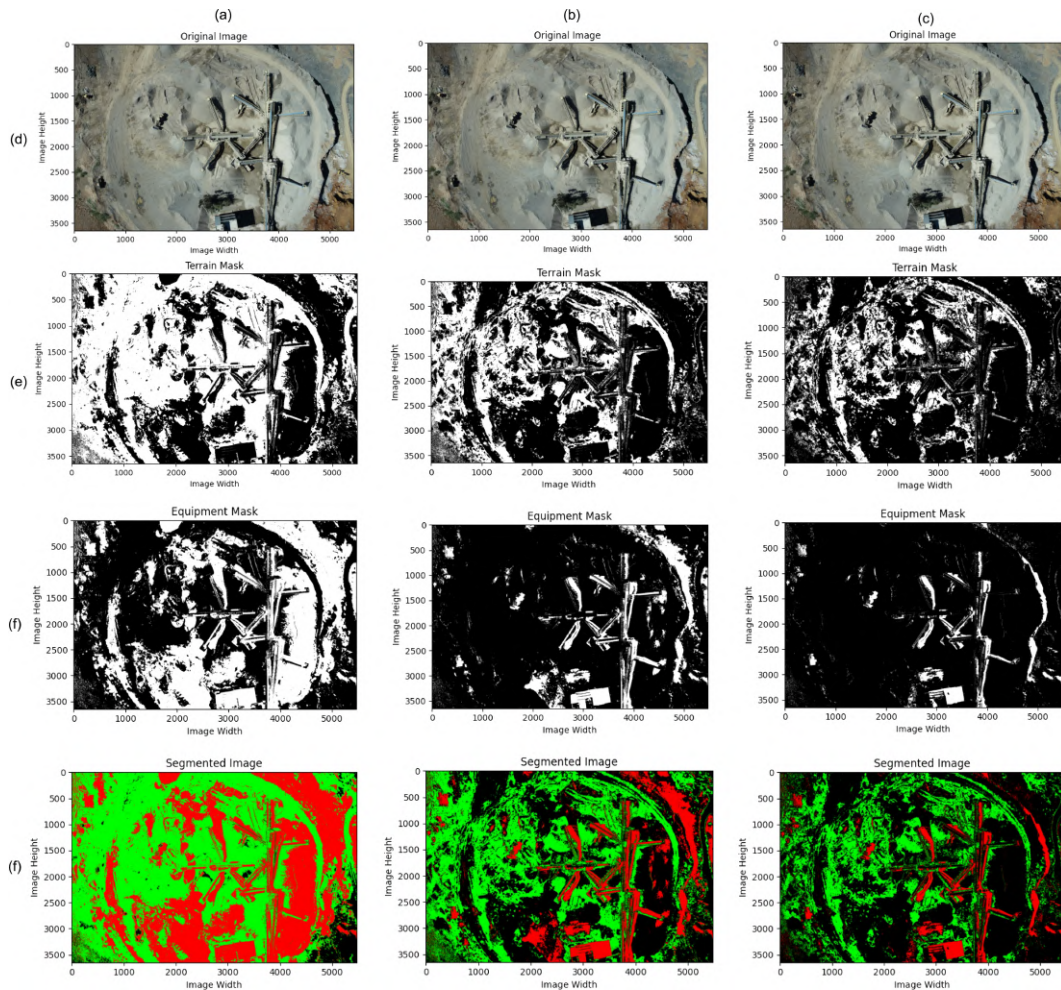


Figure 15. Displays outcomes (a) K-Means of proposed method $k=3$, (b) K-Means of proposed method $k=5$, (c) K-Means of proposed method $k=10$, (d) original image, (e) terrain mask, (f) equipment mask, (g) segmented image

The provided numbers of cluster centroids and histograms represent the analyzed results of K-Means clustering:

- Cluster Centroids: These numbers represent the centroid of the pixel within each cluster (their position). Each centroid has a coordinate of (a^*, b^*) in the LAB color space, indicating the mean values of a^* and b^* for the pixel that the cluster belongs to.
- Cluster histograms: These numbers represent the number of pixels in each cluster assigned to it. The histograms show the distribution of the pixels among the clusters.

The third step in the process is cluster analysis. Once the cluster centroids are obtained, Figure 16

represents the cluster analysis process illustrated in Figure 16 (a) for $k=3$, Figure 16 (b) for $k=5$ and Figure 16 (c) for $k=10$. Each centroid represents a different cluster, and this graphical depiction offers insights into the spatial distribution of clusters within the image. To begin, the number of distinct cluster centroids is determined as follows:

Cluster Centroids for $k=3$:

Cluster 0: [1646.18624056 2290.48363752] Cluster 1: [1955.74732017 3159.66616999]
Cluster 2: [2702.38300052 4162.48997817]

Cluster Centroids for $k=5$:

Cluster 0: [1657.79303474 2175.72433118] Cluster 1: [1954.22469208 3578.25497254]
Cluster 2: [3082.13420848 4737.49083326] Cluster 3: [1933.62125778 2870.56790236]
Cluster 4: [1597.2876867 2595.56156581]

Cluster Centroids for $k=10$:

Cluster 0: [1627.25146132 2234.87462388] Cluster 1: [2159.45221849 3359.76138389]
Cluster 2: [1770.78750289 3445.34768547] Cluster 3: [1827.46278324 3655.14051166]
Cluster 4: [1596.24838427 1708.72602408] Cluster 5: [1482.35032808 2297.1734342]
Cluster 6: [2708.63469837 2512.11796511] Cluster 7: [2022.47053219 2864.45787182]
Cluster 8: [3150.53409569 4938.33328442] Cluster 9: [2243.51326788 3643.24983779]

Following this, we proceed to visualize the cluster histograms corresponding to each segmented image. Figure 17 visually represents the three cluster histograms for $k=3$ illustrated in Figure 17(a), $k=5$ in Figure 17(b), and $k=10$ in Figure 17(c).

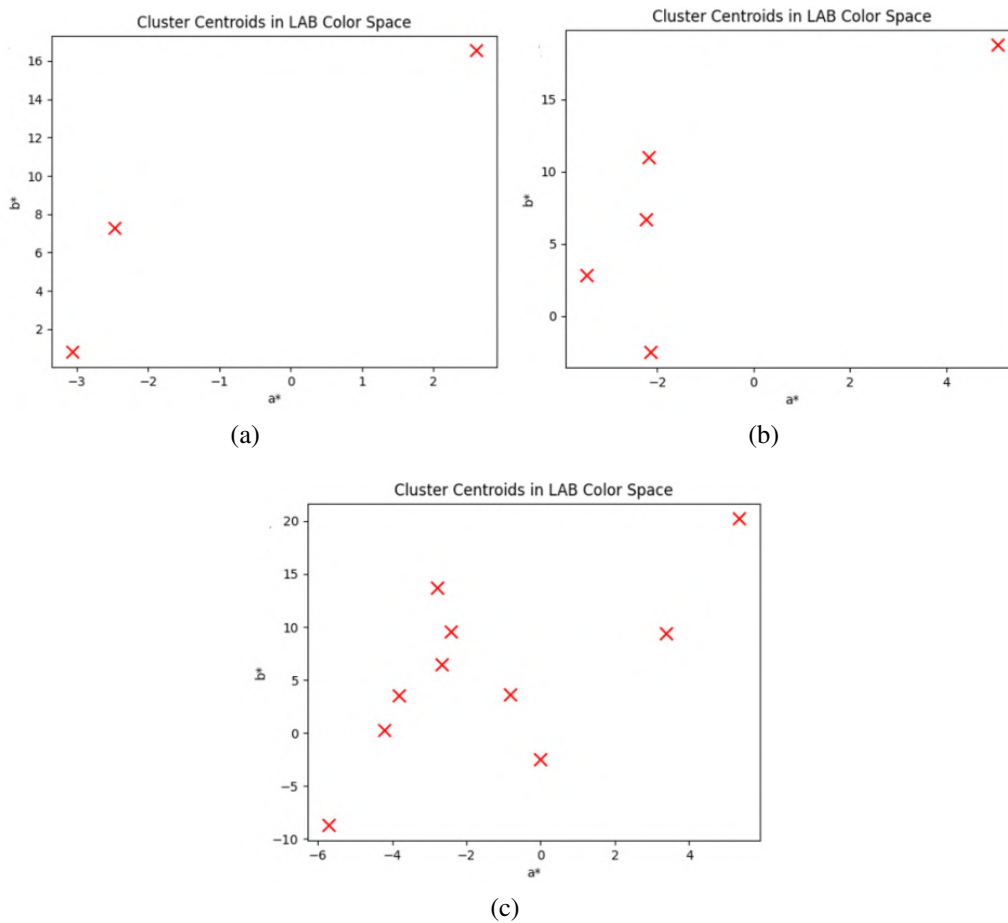


Figure 16. The cluster analysis process (a) cluster centroids $k=3$, (b) cluster centroids $k=5$, and (c) cluster centroids $k=10$

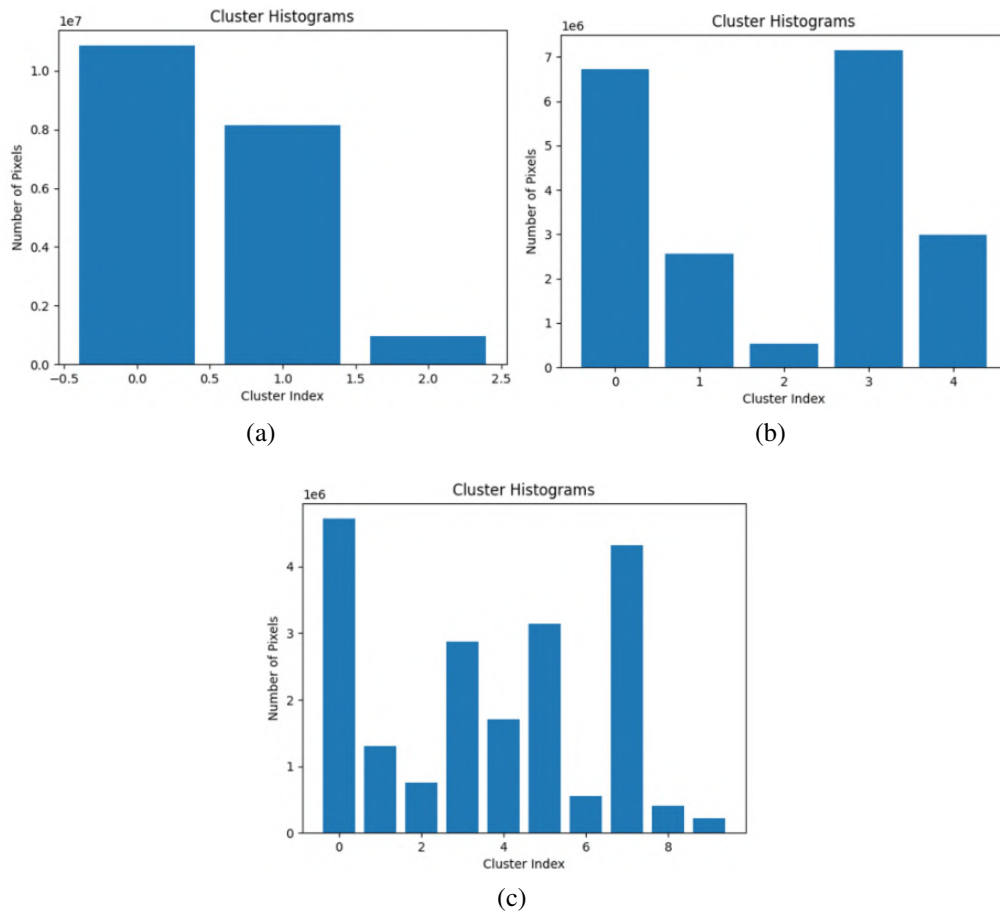


Figure 17. The three cluster histograms for: (a) $k=3$, (b) $k=5$, (c) $k=10$

Number of pixels for $k = 3$:

Cluster 0: 10854408 Cluster 1: 8142854 Cluster 2: 964594

Number of pixels for $k = 5$:

Cluster 0: 6733072 Cluster 1: 2557095 Cluster 2: 533014
 Cluster 3: 7147859 Cluster 4: 2990816

Number of pixels for $k = 10$:

Cluster 0: 4718857 Cluster 1: 1302125 Cluster 2: 747949
 Cluster 3: 2866424 Cluster 4: 1707745 Cluster 5: 3133517
 Cluster 6: 556885 Cluster 7: 4315116 Cluster 8: 402089
 Cluster 9: 211149 Interpretation:

Let's interpret the results of each k value (number of clusters) and identify which cluster appears to be the most dominant in the image.

– For $k=3$:

We have three clusters. Cluster 0 has the highest number of pixels with 10854408 pixels, followed by Cluster 1 with 8142854 pixels, and Cluster 2 with 964594 pixels. Cluster 0 is dominant in the image.

– For $k=5$:

For the five clusters, the size of the cluster varies; cluster 3 has the highest number of pixels with 7147859 pixels, followed by cluster 0 with 6733072 pixels, cluster 4 with 2990816 pixels, cluster 1 with 2557095 pixels, and then cluster 2 with 553014 pixels. This suggests that cluster 3 is the most dominant in the image.

– For $k=10$:

Based on the pixel distribution among the clusters, Cluster 0 has the highest number of pixels with 4718857, making it the most dominant cluster in the image. Following that, Cluster 7 with 4315116 and Cluster 5

with 3133517 also have significant pixel counts. Cluster 0 is the most dominant in the image but the clusters 7 and 5 are between the equipment and the terrain.

In $k=3$ and $k=5$, the terrain is the most dominant in the image. In the case of $k=10$, cluster 7 is located in the equipment part and is the second dominant in the image. In the fourth part of the proposed method, we will exploit the morphological mathematical method to extract information from segmented images of $k=3$, $k=5$, and $k=10$. Our focus is on the identification of mining equipment in the segmented regions that represent the terrain and the mining equipment. We will use the four morphological mathematical operations of erosion, dilation, opening, and closing to refine the distinct color of the equipment. Figure 18 shows the four operations of morphological mathematics on segmented images by $k=3$ shown in Figure 18 (a), $k=5$ illustrated in Figure 18 (b), and $k=10$ presented in Figure 18 (c), respectively. The presented results indicate a significant improvement in the isolation of equipment between $k=3$, $k=5$, and $k=10$. This improvement reinforces the efficiency of the approach in the mining industry and contributes to decision-making.

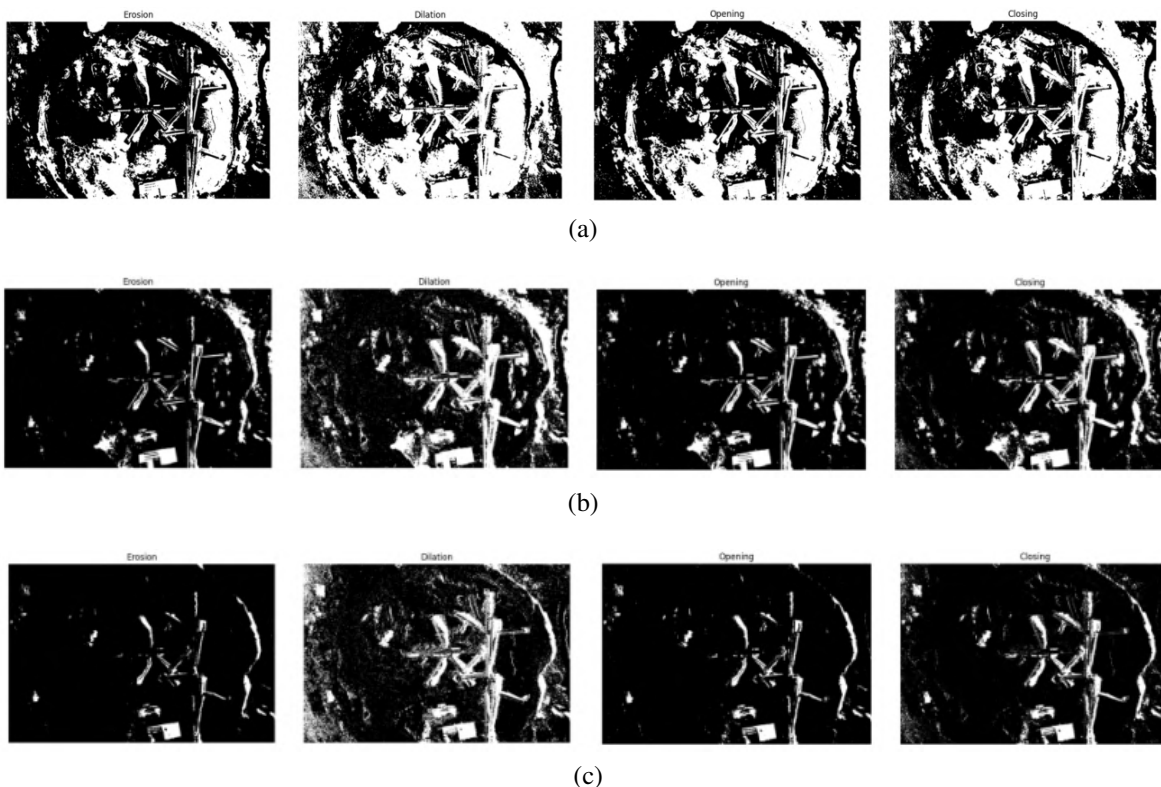


Figure 18. The four operations of morphological mathematics on segmented images: (a) the four operations results in $k=3$, (b) the operations results in $k=5$, and (c) erosion, dilation, opening, and closing results in $k=10$

The final part of the proposed method involves evaluating the segmented image of both the classical K-Means and the suggested method. This evaluation is important as it allows us to check the effectiveness and measure the performance of our approach to the segmentation objectives. To assure the relevance of a segmentation method, the evaluation of its performance is important. In this part, we will commonly use five different performance measures. The first is the Rand Index, which measures the similarity between two data segmentations [25]. The second is the Fowlkes-Mallows Index, which determines the similarity between two segmentations using the geometric mean of precision and recall [26]. The third is the peak signal-to-noise ratio, which is used to measure the quality of a segmented image by comparing it to the original image [27]. The fourth is the pearson correlation coefficient (PCC), which measures the linear correlation between two images [28], and the fifth is the Intersection over Union (IoU), which is used to evaluate the accuracy of object detection and image segmentation algorithms [29]. Those performance measures are identified by researchers as essential for the evaluation of an image segmentation method. Table 8 presents the mathematical

formulations or performance parameters used for evaluating segmentation methods.

Note:

- $(2^b - 1)$ represents the maximum value of possible pixels on an image.
- MSE is a measure of the average squared difference between pixels in the original and processed image.
- In intersection over union, X and Y represent the pixel positions in the image.
- In PSNR, “b” represents the number of bits used to represent each pixel.

Table 8. Mathematical formulations for the evaluation of image segmentation method

Name of the parameter	Formulations
Rand index (RI)	$RI = \frac{a+d}{a+b+c+d}$
Fowlkes-mallows index (FMI)	$FMI = \sqrt{\text{Precision} \times \text{Recall}}$
Peak signal-to-noise ratio (PSNR)	$PSNR = 10 \log_{10} \left(\frac{(2^b - 1)^2}{\sqrt{MSE}} \right)$
Pearson correlation coefficient (PCC)	$R = \frac{\sum_{i=1}^n (X_i - \bar{X})(Y_i - \bar{Y})}{\sqrt{\sum_{i=1}^n (X_i - \bar{X})^2 \sum_{i=1}^n (Y_i - \bar{Y})^2}}$
Intersection over union (IoU)	$IoU = \frac{ X \cap Y }{ X + Y }$

Among the parameters mentioned, a higher value means better segmentation. The ground truth mask we have established corresponds to the mining equipment for the three cases (k=3, k=5, and k=10). These ground truth masks serve as a reference for evaluating the quality of the segmentation results. Our evaluation will be structured into three tables. Table 9 will display the results of the five evaluation methods used on the classic K-Means clustering algorithm in three images: one with k=3, another with k=5, and a third one with k=10. Table 10 will present the evaluation results of the proposed method for the opening operation, while Table 11 will show the results for the closing operation. The rand index (RI), fowlkes mallows index (FMI), peak signal to noise ratio (PSNR), pearson correlation coefficient (PCC), and intersection over union (IoU) values are calculated for the K-Means clustering classic as well as the proposed method for the three different images of K (3, 5, and 10). Our analysis revealed across the five evaluation parameters that the performance of the proposed method in K=3, K=5, and 10 displayed higher values in all the parameters except for the peak signal noise ratio (K=3), where it scored 4.486 in the opening and 4.730 in the closing compared to the K-Means classic, which scored 5.192. This means that, for k=3, the classical K-Means show better PSNR.

Table 9. Evaluation results of K-Means classic

Image	Rand index	Fowlkes Mallows	Peak Signal to Noise ratio	Pearson Correlation	Intersection over Union
K=3	0.0142	0.4419	5.192	0.2030	0.2201
K=5	0.0245	0.4785	4.864	0.4742	0.0307
K=10	0.0112	0.3605	4.905	0.0262	0.0022

Table 10. Evaluation results of the proposed method for opening

Image	Rand Index	Fowlkes Mallows	Peak Signal to Noise Ratio	Pearson Correlation	Intersection over Union
K=3	0.03877	0.6464	4.486	0.2772	0.1227
K=5	0.37793	0.8797	11.121	-0.0683	0.3894
K=10	0.62771	0.9485	18.009	-0.0475	0.7533

Table 11. Evaluation results of the proposed method for closing

Image	Rand Index	Fowlkes Mallows	Peak Signal to Noise Ratio	Pearson Correlation	Intersection over Union
K=3	0.08419	0.6421	4.730	-0.8265	0.1921
K=5	0.51710	0.8907	11.356	-0.0683	0.4949
K=10	0.73938	0.9545	15.879	-0.0475	0.7113

Analyzing the differences between the closing and opening operations of the proposed method from the results, the closing (K=10) is better regarding the three first evaluation methods, and the opening is better in terms of peak signal noise ratio (PSNR) indicating a better image reconstruction quality. If we are looking for cluster matching and segmentation quality, the closing operation is preferable, and if we are looking for

reconstructing the image, the opening operation is better. Pearson's correlation seems to be less informative in both cases.

4.5. Discussion

In our study, three different images of k-value were selected to conduct the image segmentation. This allowed us to explore numerous levels of segmenting the mining equipment images. Our approach, compared with the previous studies, shows an improvement in the effectiveness of our method. Maybe a large value of K will introduce some noise and affect the segmentation. Our research holds significant implications for mining operators, leading to improvements in equipment recognition and monitoring. The proposed method offers more accurate and efficient segmentation than the K-Means classic, which is a critical task, especially for equipment maintenance, tracking, and operator safety. There is only one limitation in our method: we observed that shadows have resulted in a building structure as part of the equipment. This needs further refinement to improve the accuracy of the segmentation and in the world of advanced technology, the Internet of Things is often used to resolve those issues [30], [31]. In Table 12, we present a comparative analysis of various image segmentation methods, including the proposal approach (referred to as this work) and several methods from recent articles.

Table 12. Comparative analysis of different segmentation methods

Variable	This Work	[32] (2023)	[33] (2023)	[34] (2021)	[35] (2021)	[36] (2018)
Segmentation	K-Means+ Morphology	EMO Kapur	UNET+ SqueezeUNET	TPLMM- K-Means	Otsu + lebTLBO	Adaptive K-Means
IoU	0.7113	-	0.68	-	0.5573	0.642708
PSNR	15.879	20.4749	11.94	14.323	58.75	-
Rand Index	0.73938	0.6867	-	0.9190	-	-
Dataset	MineCareerDB (373 images)	No Dataset	OCHuman Dataset	COG Dataset	ALL IDB (366 images)	No Dataset
Application	Mining Industry	Satellite Imagery	Human Detection	Medical	Medical	Food
Limitation	Shadows	Sensitivity	Occlusion	-	Limited dataset info	Time Running
Color Model	CIELAB	RGB	RGB	RGB	RGB	CIELAB

In the comparative analysis, our proposed hybrid segmentation method stands out for its accuracy (IoU: 0.7113). The optimized K determination approach enhances computational efficiency, addressing challenges associated with shadows in mining applications. However, the method's running time could be a potential area for improvement. While the method (Otsu+letTLBO) [35] achieved a high segmentation quality with PSNR (58.75), it admits a limitation in dataset information. Method (TPLMM-K-Means) [34] showcases robust clustering performance with a high Rand index (0.9190) and a focus on COG datasets. On the other hand, Method (EMO Kapur) [32] highlights the need for sensitivity improvements in real-world scenarios. The choice of K-Means clustering in our processing chain is due to its proven effectiveness in image segmentation tasks and its simplicity, speed, and versatility. Because it applies to various types of image data, its non-parametric nature makes it adaptable to different characteristics present in diverse datasets, making it well-suited for comparison with the proposed hybrid method. While there are various clustering approaches available, such as hierarchical clustering [37] or density-based spatial clustering of applications with noise (DBSCAN) [38], we use K-Means for its clear interpretability and ability to handle large datasets.

5. CONCLUSION

In this article, we carried out a comprehensive analysis using a dataset of 373 images from the study site. These images were perfectly transformed into a 3D point cloud representation and examined in the tree viewer to facilitate the identification of the region of interest and to check for the quality of the dataset, and we carried out root mean square error to check the missed data points. In addition, we proposed an improvement to K-Means clustering by adding the mathematical morphology. We then subjected the results of our proposed method to comparison with the classic K-Means. Their comparative analysis is supported by using various evaluation methods such as the Rand index, Fowlkes Mallows index, pearson correlation, peak signal noise

ratio, and intersection over union. Wrapping up our study, we carefully compared our segmented method with different recent articles spotlighting its strengths and advancements. This analysis provides valuable insights into the distinctive contribution of the approach to the current field of segmentation research, making it a crucial benchmark. Those measures were used as an objective to evaluate our proposed approach. We concluded that our suggested method outperforms the K-Means classic. This underlines the potential of our methodology to improve the quality of image segmentation in mining tasks. The methodology employed in this work could be extended to facilitate fine-grained classification within the mining sector, providing a more nuanced understanding of equipment types and structural components. The integration of neural network-based object detection algorithms could improve our approach by identifying and localizing individual objects in the mining environment. In summary, our research introduces a method that we believe enhances mining operations by optimizing their strategies and making a more efficient decision-making process.




REFERENCES

- [1] G. K. Moore, "What is a picture worth? a history of remote sensing," *Hydrological Sciences Bulletin*, vol. 24, no. 4, pp. 477–485, 1979, doi: 10.1080/02626667909491887.
- [2] S. Lee and Y. Choi, "Reviews of unmanned aerial vehicle (drone) technology trends and its applications in the mining industry," *Geosystem Engineering*, vol. 19, no. 4, pp. 197–204, 2016, doi: 10.1080/12269328.2016.1162115.
- [3] A. Rejeb, A. Abdollahi, K. Rejeb, and H. Treiblmaier, "Drones in agriculture: a review and bibliometric analysis," *Computers and Electronics in Agriculture*, vol. 198, 2022, doi: 10.1016/j.compag.2022.107017.
- [4] G. Rohi, O. Ejofodomi, and G. Ofualagba, "Autonomous monitoring, analysis, and countering of air pollution using environmental drones," *Heliyon*, vol. 6, no. 1, 2020, doi: 10.1016/j.heliyon.2020.e03252.
- [5] H. Ren, Y. Zhao, W. Xiao, and Z. Hu, "A review of UAV monitoring in mining areas: current status and future perspectives," *International Journal of Coal Science and Technology*, vol. 6, no. 3, pp. 320–333, 2019, doi: 10.1007/s40789-019-00264-5.
- [6] B. Lei, N. Wang, P. Xu, and G. Song, "New crack detection method for bridge inspection using UAV incorporating image processing," *Journal of Aerospace Engineering*, vol. 31, no. 5, 2018, doi: 10.1061/(asce)as.1943-5525.0000879.
- [7] J. Lööv, L. Abrahamsson, and J. Johansson, "Mining 4.0—the impact of new technology from a work place perspective," *Mining, Metallurgy and Exploration*, vol. 36, no. 4, pp. 701–707, 2019, doi: 10.1007/s42461-019-00104-9.
- [8] G. Esposito, G. Mastroiocco, R. Salvini, M. Oliveti, and P. Starita, "Application of UAV photogrammetry for the multi-temporal estimation of surface extent and volumetric excavation in the Sa Pigada Bianca open-pit mine, Sardinia, Italy," *Environmental Earth Sciences*, vol. 76, no. 3, pp. 1–16, 2017, doi: 10.1007/s12665-017-6409-z.
- [9] N. Uzakkyzy et al., "Image noise reduction by deep learning methods," *International Journal of Electrical and Computer Engineering (IJECE)*, vol. 13, no. 6, pp. 6855–6861, 2023, doi: 10.11591/ijece.v13i6.pp6855-6861.
- [10] H. S. Waskale and M. Bhong, "Experimental RGB and CIE lab colour space analysis and comparison for fruits and vegetables," *Journal of Emerging Technologies and Innovative Research*, vol. 4, no. 4, pp. 1–4, 2017.
- [11] N. Haqiq, M. Zaim, M. Sbihi, M. El Alaoui, L. Masmoudi, and H. Echarrafi, "Mine4.0 - MineCareerDB: A mining career dataset - Mendeley Data," *Mendeley Data*, V3, 2024, doi: 10.17632/c5s76mj4bm.3
- [12] "Agisoft metashape," Agisoft, <https://www.agisoft.com/downloads/installer/>, (accessed Apr 25, 2023).
- [13] M. Isenburg, "LASzip: lossless compression of lidar data," *Photogrammetric Engineering and Remote Sensing*, vol. 79, no. 2, pp. 209–217, Feb. 2013, doi: 10.14358/PERS.79.2.209.
- [14] M. Schütz, "Potree viewer," <https://github.com/potree/potree/releases/> (accessed May 02, 2023).
- [15] M. Schuetz, "Potree Converter," 2017. <https://github.com/potree/PotreeConverter> (accessed Jun. 28, 2023).
- [16] M. Schütz, S. Ohrhallinger, and M. Wimmer, "fast out-of-core octree generation for massive point clouds," *Computer Graphics Forum*, vol. 39, no. 7, pp. 155–167, Oct. 2020, doi: 10.1111/cgf.14134.
- [17] J. Marešová et al., "Applicability of data acquisition characteristics to the identification of local artefacts in global digital elevation models: comparison of the copernicus and tandem-x dems," *Remote Sensing*, vol. 13, no. 19, 2021, doi: 10.3390/rs13193931.
- [18] J. Martins, D. A. Sant'Ana, J. M. Junior, H. Pistori, and W. N. Goncalves, "Aerial image segmentation in urban environment for vegetation monitoring," in *2020 IEEE Latin American GRSS and ISPRS Remote Sensing Conference (LAGIRS)*, Mar. 2020, pp. 375–379, doi: 10.1109/LAGIRS48042.2020.9165618.
- [19] R. Barnes, "RichDEM: High-performance terrain analysis," *PeerJ Preprints*, 2018, doi: 10.7287/PEERJ.PREPRINTS.27099V1.
- [20] G. S. Bhunia, P. K. Shit, and R. Maiti, "Comparison of GIS-based interpolation methods for spatial distribution of soil organic carbon (SOC)," *Journal of the Saudi Society of Agricultural Sciences*, vol. 17, no. 2, pp. 114–126, 2018, doi: 10.1016/j.jssas.2016.02.001.
- [21] R. Vallejos, J. Pérez, A. M. Ellison, and A. D. Richardson, "A spatial concordance correlation coefficient with an application to image analysis," *Spatial Statistics*, vol. 40, 2020, doi: 10.1016/j.spasta.2019.100405.
- [22] H. Yao, Q. Duan, D. Li, and J. Wang, "An improved K-Means clustering algorithm for fish image segmentation," *Mathematical and Computer Modelling*, vol. 58, no. 3–4, pp. 790–798, 2013, doi: 10.1016/j.mcm.2012.12.025.
- [23] M. N. Qureshi and M. V. Ahamad, "An improved method for image segmentation using K-Means clustering with neutrosophic logic," *Procedia Computer Science*, vol. 132, pp. 534–540, 2018, doi: 10.1016/j.procs.2018.05.006.
- [24] S. Jardim, J. António, and C. Mora, "Graphical image region extraction with K-Means clustering and watershed," *Journal of Imaging*, vol. 8, no. 6, 2022, doi: 10.3390/jimaging8060163.
- [25] A. C. Sobieranski, D. D. Abdala, E. Comunello, and A. von Wangenheim, "Learning a color distance metric for region-based image segmentation," *Pattern Recognition Letters*, vol. 30, no. 16, pp. 1496–1506, 2009, doi: 10.1016/j.patrec.2009.08.002.
- [26] A. Rachwał et al., "Determining the quality of a dataset in clustering terms," *Applied Sciences*, vol. 13, no. 5, Feb. 2023, doi: 10.3390/app13052942.
- [27] N. Dhanachandra, K. Manglem, and Y. J. Chanu, "Image segmentation using K-Means clustering algorithm and subtractive cluster-




- ing algorithm,” *Procedia Computer Science*, vol. 54, pp. 764–771, 2015, doi: 10.1016/j.procs.2015.06.090.
- [28] R. Sammouda and A. El-Zaart, “An optimized approach for prostate image segmentation using K-Means clustering algorithm with elbow method,” *Computational Intelligence and Neuroscience*, 2021, doi: 10.1155/2021/4553832.
- [29] P. Shan, “Image segmentation method based on K-mean algorithm,” *Eurasip Journal on Image and Video Processing*, vol. 2018, no. 1, pp. 1–9, 2018, doi: 10.1186/s13640-018-0322-6.
- [30] V. Muneeswaran, P. Nagaraj, and M. F. Ijaz, “An articulated learning method based on optimization approach for gallbladder segmentation from MRCP images and an effective IoT based recommendation framework,” in *Studies in Computational Intelligence*, vol. 1021, S. Mishra, A. González-Briones, A. K. Bhoi, P. K. Mallick, and J. M. Corchado, Eds. Cham: Springer International Publishing, 2022, pp. 165–179.
- [31] K. M. Hosny, A. Magdi, A. Salah, O. El-Komy, and N. A. Lashin, “Internet of things applications using Raspberry-Pi: a survey,” *International Journal of Electrical and Computer Engineering (IJECE)*, vol. 13, no. 1, pp. 902–910, 2023, doi: 10.11591/ijece.v13i1.pp902-910.
- [32] S. Rangu, R. Veramalla, S. R. Salkuti, and B. Kalagadda, “Efficient approach to color image segmentation based on multilevel thresholding using EMO algorithm by considering spatial contextual information,” *Journal of Imaging*, vol. 9, no. 4, 2023, doi: 10.3390/jimaging9040074.
- [33] M. J. Lahgazi, P. Argoul, and A. Hakim, “Improving pedestrian segmentation using region proposal-based CNN semantic segmentation,” *Mathematical Modeling and Computing*, vol. 10, no. 3, pp. 854–863, 2023, doi: 10.23939/mmc2023.03.854.
- [34] K. V. Satyanarayana, N. T. Rao, D. Bhattacharyya, and Y. C. Hu, “Identifying the presence of bacteria on digital images by using asymmetric distribution with K-Means clustering algorithm,” *Multidimensional Systems and Signal Processing*, vol. 33, no. 2, pp. 301–326, 2022, doi: 10.1007/s11045-021-00800-0.
- [35] N. M. Deshpande, S. Gite, B. Pradhan, K. Kotecha, and A. Alamri, “Improved Otsu and Kapur approach for white blood cells segmentation based on LebTLBO optimization for the detection of Leukemia,” *Mathematical Biosciences and Engineering*, vol. 19, no. 2, pp. 1970–2001, 2022, doi: 10.3934/mbe.2022093.
- [36] X. Zheng, Q. Lei, R. Yao, Y. Gong, and Q. Yin, “Image segmentation based on adaptive K-Means algorithm,” *Eurasip Journal on Image and Video Processing*, vol. 2018, no. 1, pp. 1–10, 2018, doi: 10.1186/s13640-018-0309-3.
- [37] A. S. Kini, P. K. V. Reddy, and S. N. Pai, “Techniques of deep learning and image processing in plant leaf disease detection: a review,” *International Journal of Electrical and Computer Engineering (IJECE)*, vol. 13, no. 3, pp. 3029–3040, 2023, doi: 10.11591/ijece.v13i3.pp3029-3040.
- [38] E. M. Cherrat, R. Alaoui, and H. Bouzahir, “Improving of fingerprint segmentation images based on K-Means and DBSCAN clustering,” *International Journal of Electrical and Computer Engineering (IJECE)*, vol. 9, no. 4, pp. 2425–2432, 2019, doi: 10.11591/ijece.v9i4.pp2425-2432.

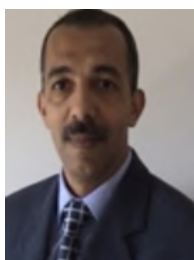
BIOGRAPHIES OF AUTHORS






Nasreddine Haqiq    was born in Rabat on september 30, 1998. He received a B.Eng. degree in computer science and management systems from the School of Textile and Clothing Industries (ESITH) in Casablanca, Morocco, in 2021. Currently, he is a Ph.D. student in the LASTIMI Research lab (Laboratory of System Analysis, Data Processing, and Integrated Management). His research interests include internet of things systems, artificial intelligence, image processing, computer vision, industrial applications, machine learning, and deep learning. He can be contacted at email: nasreddine_haqiq@um5.ac.ma.






Mounia Zaim    was born in Fes on July 19, 1973. She received a B.S. in engineering science from University Mohammed V, Rabat, in 1996, an M.S. in telecommunications and microwaves from University Chouaib Doukkali, El-Jadida, in 1997, and a Ph.D. degree in computer vision from University Sidi Mohammed Ben Abdellah, Fes, in 2002. She is currently a professor in the higher Institute of Technology SALE, since 2003 and a member of the Research Lab LASTIMI (Laboratory of System Analysis, data processing and Integrated Management). Her fields of interest are computer vision, data analysis, industry 4.0 tools, and artificial intelligence. She can be contacted at email: mounia.zaim@est.um5.ac.ma






Mohamed Sbihi    was born in Rabat on 22/11/1962, is a full professor of Higher Education. He received a Graduate Degree in electronics and signal Processing from the Faculty of Science at the Mohammed V University in Rabat in 1995, and a Ph.D. in automatic and information processing from the Faculty of Science at Ibn Tofail University in Kenitra 2006. He has been employed since 1996 and member of the Laboratory of System Analysis, Information Processing and Industrial Management in the Superior School of Technology in SALE at Mohammed V University in Rabat, Morocco. He works on image processing, data analysis, university teaching embedded systems, and robotics. He can be contacted at email: mohammed.sbihi@est.um5.ac.ma






Mustapha El Alaoui    born in the Old Medina of Fes, Morocco, in 1994. He achieved his Master's degree in micro-electronics from the Faculty of Sciences Dhar EL Mahraz (FSDM), Sidi Mohammed Ben Abdellah University (USMBA), Fez, Morocco, in 2017. In 2021, he successfully completed his Ph.D. in electrical engineering at the Laboratory of Computer Science, Signals, Automation, and Cognitivism (LISAC), Department of Physics, FSDM, USMBA, Fez, Morocco. Currently serving as a Professor in the Physics Department at the Faculty of Science, Mohammed V University in Rabat, Morocco. His diverse research interests encompass a broad spectrum of topics, including Li-Ion battery charger interface (BCI) and battery management systems (BMS), both passive and active RFID tags, CMOS mixed-mode integrated circuit design, integrated class-D power output stage, renewable energy, embedded systems, precision agriculture, and smart farming. He can be contacted at email: m.elalaoui@um5r.ac.ma.



Lhoussaine Masmoudi    received the Ph.D. degree in computer vision, from the University of Valladolid (Spain), in 1994. A master degree in automatic and signal processing, from the University Sidi Mohamed Ben Abdellah, Fes (Morocco), in 1988. And, bachelor electronic degree from the Mohammed V University of Rabat, Faculty of Sciences, Rabat (Morocco), in 1985. He is currently Professor at the University Mohammed V of Rabat, Faculty of Sciences, Physics Department, Rabat (Morocco). His research interests include computer vision and image processing. He can be contacted at email: lhmasmoudi@gmail.com, l.masmoudi@um5r.ac.ma



Hamza Echarrafi    is the CEO and co-founder of Morocco General Company of Geomatics (SGMG). He received his license fundamental in geological and universe options of hydrology and pedology from the University of Chouaib Doukkali (EL JADIDA) in 2017. A master's degree in geomatics applied in geosciences and environment from the University Hassan II, Casablanca (Morocco), in 2019. His research interests include geomatics, 3D mapping, and photogrammetry. He can be contacted at email: echarrafi01hamza@gmail.com